Instability Measurements in the Boeing/AFOSR Mach-6 Quiet Tunnel

Joshua B. Edelman,[*] Brandon C. Chynoweth,[*] Gregory R. McKiernan,[*]
Cameron J. Sweeney,[*] and Steven P. Schneider[†]
School of Aeronautics and Astronautics
Purdue University
West Lafayette, IN 47907-1282

A new 7° half-angle cone at 6° angle of attack was used to investigate the growth of secondary instabilities on hypersonic stationary crossflow waves. The new cone allows rotation of the sensor array before each run, independently of the rest of the cone. Good repeatability of the cone flow with respect to rotation was established. Measurements of secondary instabilities show the existence of at least two modes, each maximum in different areas of the stationary vortex. Experiments were also performed on a 30° half-angle cone probe equipped with two different pressure transducers to measure the disturbance level of a Mach 6 Ludweig Tube and compare the disturbance levels measured to another facility. It was found that the low frequency disturbance levels differed greatly between the two facilities. Third, RIM insert with 45 roughness elements was tested on a flared cone geometry. Peak second-mode pressure fluctuations of nearly 35% were measured, similar to previous results with a smooth wall. Temperature sensitive paint measurements showed a modified hot-cold-hot heating pattern. Fourth, preliminary measurements on a 7° half angle cone with a slice and flap were made to study free-shear layer transition in a low noise environment. Boundary-layer transition within the free-shear layer has been observed and is altered by the freestream noise levels.

Nomenclature

f	frequency
M	Mach number
p	pressure
p_0	stagnation pressure
θ	azimuthal angle
$\dot{q}$	heat flux
Re	Reynolds number based on sensor axial distance
Re_∞	unit Reynolds number
T	temperature
T_0	stagnation temperature
t	time

x	model axial coordinate
z	distance from tunnel throat

Abbreviations

BAM6QT	Boeing/AFOSR Mach-6 Quiet Tunnel
HLB	Hypersonic Ludweig Tube, Technische Universität Braunschweig
TSP	Temperature-Sensitive Paint
PSD	Power-Spectral Density
RIM	Rod Insertion Method

---

[*]Research Assistant. Student Member, AIAA
[†]Professor. Associate Fellow, AIAA

I. Introduction

A. Hypersonic Boundary Layer Transition

An accurate understanding of boundary-layer transition is vital to the design of hypersonic vehicles. The state of the boundary layer directly affects the vehicle's aerodynamics and heating loads. However, the mechanisms of high-speed boundary layer transition are not well understood. An important tool in understanding the processes of transition is the quiet tunnel. A high freestream noise level can cause early transition, or even change the responsible mechanisms. Conventional wind tunnels have freestream noise levels of around 1% or greater. Freestream noise levels in flight are orders of magnitude smaller. Quiet tunnels produce freestream noise around 0.05% or less, allowing the study of boundary-layer transition in a flight-like noise environment.

B. The Boeing/AFOSR Mach-6 Quiet Tunnel

The Boeing/AFOSR Mach-6 Quiet Tunnel (BAM6QT) is one of three hypersonic quiet tunnels in the world. A schematic of the BAM6QT is provided in Figure 1. The BAM6QT is a Ludwieg tube composed of a long driver tube, a converging-diverging nozzle, and a large vacuum tank. To operate the BAM6QT, first a pair of diaphragms are placed between the diffuser and the vacuum tank as indicated in Figure 1, and the pressure in the driver tube is increased to the desired value. To make a run, the diaphragms are burst, causing a shock to propagate downstream into the vacuum tank and an expansion fan to propagate upstream through through the nozzle, starting the wind tunnel. The expansion fan reflects between the two ends of the driver tube, causing a stagnation pressure drop of about 1% per reflection. Each cycle lasts about 200 ms. During the reflection cycle the stagnation pressure is quasi-constant.
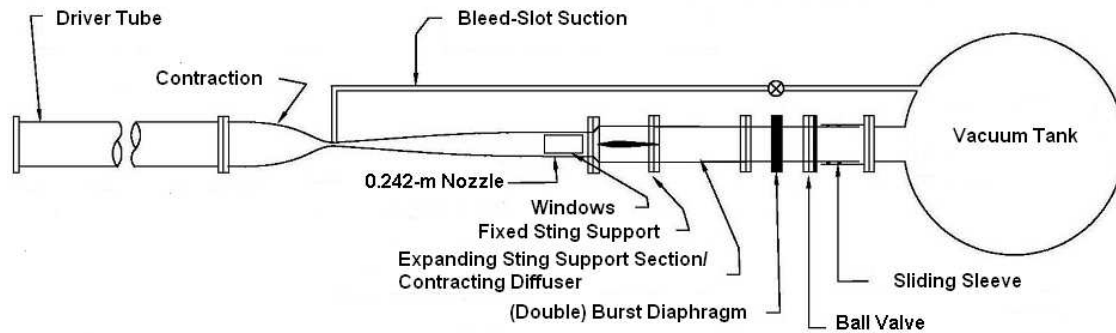

Figure 1. A schematic of the Boeing/AFOSR Mach-6 Quiet Tunnel.

The BAM6QT has several design features which keep the boundary layer laminar on the nozzle walls. The nozzle expansion section is polished to a mirror finish, and is very long to reduce the growth of the Görtler instability. In addition, the boundary layer in the contraction is removed through a bleed slot just before the throat, enabling a fresh laminar boundary layer to form in the nozzle expansion. In this configuration, the BAM6QT can run at unit Reynolds numbers up to 12.7×10^6 /m with freestream noise levels around 0.05% or lower. Additionally, if the bleed slot at the throat is not used, the BAM6QT can be run as a conventional tunnel with noise levels near 3%.

2

II.   Secondary Instabilities of the Hypersonic Stationary Crossflow Wave

The crossflow instability is often responsible for boundary-layer transition in three-dimensional flow fields, such as swept wings, lifting bodies, and cones at an angle of attack. On a sharp cone at an angle of attack in hypersonic flow, the shock is stronger near the windward ray than the leeward ray. This creates a circumferential pressure gradient from the wind side to the lee side. The pressure gradient affects the low momentum fluid close to the wall more than the outer flow, creating a crossflow component of the boundary layer flow perpendicular to the outer inviscid flow. The crossflow component has an inflection point and is therefore inviscidly unstable. Crossflow instabilities manifest as either stationary or traveling waves. In low-noise environments like those of flight, stationary waves appear to dominate the transition process.[1]

One path to turbulence is through secondary instabilities of the stationary vortices. These have been well studied for low-speed flows mostly on swept wings,[2–5] and are beginning to be observed and computed at high speeds on sharp cones.[6–8] At low speeds, a transition correlation based on N-factors of the secondary instabilities yields better results than correlations based on the stationary crossflow wave growth alone.[4] If this remains true at high speeds and a transition-prediction criterion can be formed from high-speed secondary-instability data, it would be a valuable tool for designers of hypersonic vehicles.

A.   Rotatable Cone Model

As in previous experiments,[9] a 7° half-angle cone at 6° angle of attack was used to measure the secondary instabilities. The Rotatable Cone incorporates several changes to previous models to make more refined and consistent measurements. A schematic of this cone is provided in Fig. 2. All of the cone is aluminum except the center shaft and the nosetip, which are stainless steel. The nosetip is nominally sharp with a nose radius of about 80 μm.

The total length of the Rotatable Cone is about 0.4 m (16 in), with a base diameter of 0.1 m (3.92 in). The unique feature of the Rotatable Cone is the ability of the sensor frustum to rotate independently of the rest of the cone. This feature and the cone design were inspired by Muñoz et al.[10] The new cone uses the same nosetip and can use the same dimpled Torlon roughness inserts as previous models.[9] In addition, the new cone can use RIM inserts, modeled after those of Chynoweth,[11] which provide more consistent roughness properties. The Rotating cone has a high density grid of 16 PCB132A31 pressure sensors arranged along four rays. The sensor array extends from 0.335 m (13.1 in) to 0.376 m (14.8 in) axially from the nosetip. An Schmidt-Boelter heat-transfer gauge is placed at 0.26 m (10.1 in). Each sensor ray is offset 6° from the previous ray. Each sensor is 12.7 mm (0.5 in) axially from the previous sensor, with the first and third row offset 6.4 mm (0.25 in) behind the second and fourth rows.

A rotatable sensor array solves two of the major issues with the previous models. First, the azimuthal resolution of the sensors is increased, estimated as ±0.5°. More importantly, a sensor can be rolled underneath a stationary vortex without changing the vortex significantly. Using previous models, rotating a sensor underneath a vortex involved rotating the entire model including the roughness insert. When the roughness insert is rotated, each roughness element sees a different flowfield, which changes the initial formation of the stationary vortices and their subsequent development. For the Rotatable Cone, the roughness insert is always in the same position, meaning sensors can be rotated freely without changing the initial development of the vortices. Using the Rotatable Cone, the azimuthal extent of the secondary instabilities can be investigated with more confidence and better repeatability.

The PCB data were sampled at 5 MHz using Tektronix oscilloscopes in Hi-Res mode. The power spectral densities and coherences were calculated from 0.1 s segments using Welch's method with a frequency resolution of 2500 Hz and an overlap of 50%. A CFD solution of the laminar flow, with a 300 K wall temperature, was calculated using US3D by Jeff Rigney. The measured pressure data is normalized by the CFD edge pressure at the same azimuthal location as the PCB in question.
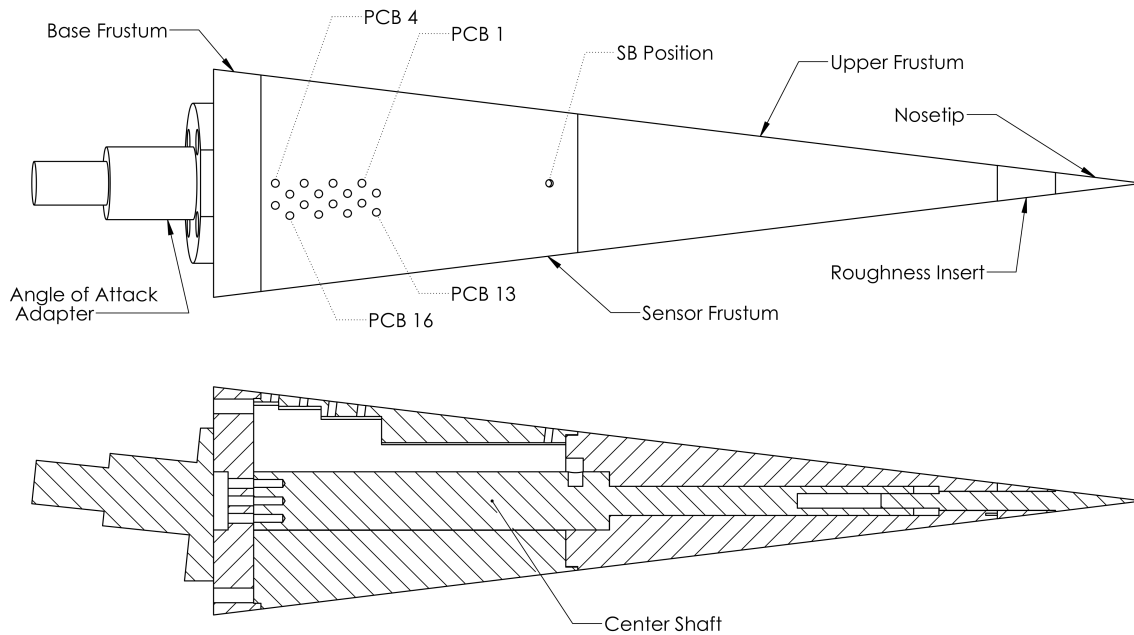
3

Figure 2. A schematic of the Rotatable Cone.
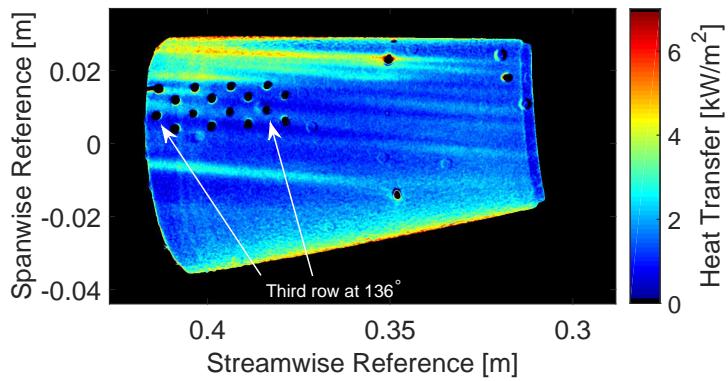
B. Rotation Repeatability

Before data can be confidently collected using the Rotatable Cone, it is important to show that rotating the sensor frustum does not significantly affect the measured data. If the junction between the sensor frustum and the upper frustum is not uniform, rotating the sensors could change the development of the stationary crossflow waves and therefore also the secondary instabilities. In addition, rotating the sensor frustum changes the random paint roughness and the upstream paint-step profile. To determine the effect of these changes, data were collected before and after rotating the sensor frustum by 12°. The first and third row of PCBs are offset by 12° azimuthally, so the first row measurements before the rotation should be the same as the third row measurements after the rotation. This is also true of the second and fourth rows, respectively.

Figure 3 shows the TSP-inferred heat-transfer images of the two runs used to examine the rotation repeatability. Qualitatively, they are similar. The streaks appear in roughly the same places for both runs. However, the heat transfer magnitudes are quite different. This could be a physically real effect, or it could be due to uncertainties in the heat-transfer calibration process.

Given the uncertainties inherent in the TSP reduction, the PCB power spectra are more useful in determining repeatability between the runs. Figure 4 provides five comparisons between PCBs during the two runs. Figures 4(a-d) compare the first and third rows, each measured at 136° from the windward ray. Figure 4(f) is a comparison between the farthest downstream sensor on the second and fourth rows, at 130°. Because the initial tunnel conditions (provided in Table 1) were slightly different between the two runs, data was taken from different times in each run when the freestream unit Reynolds number is the same.

4
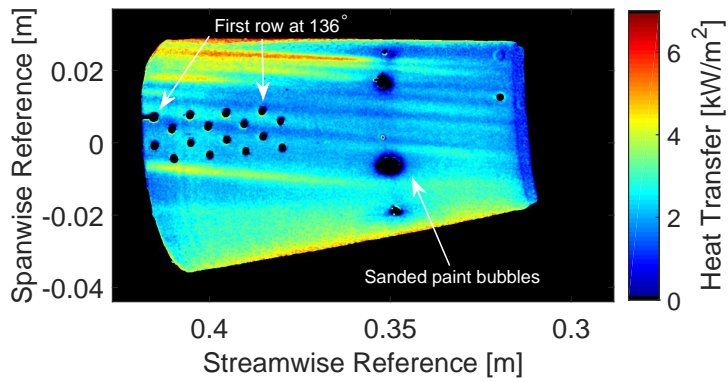
(a) Run 505. First row at $136°$, third row at $124°$. $Re_\infty = 10.9 \times 10^6$ /m.

(b) Run 504. First row at $148°$, third row at $136°$. $Re_\infty = 10.9 \times 10^6$ /m.

Figure 3. The two runs used to examine rotating repeatability with the new cone. The dark patches at 0.35 m are paint bubbles that have been sanded smooth.
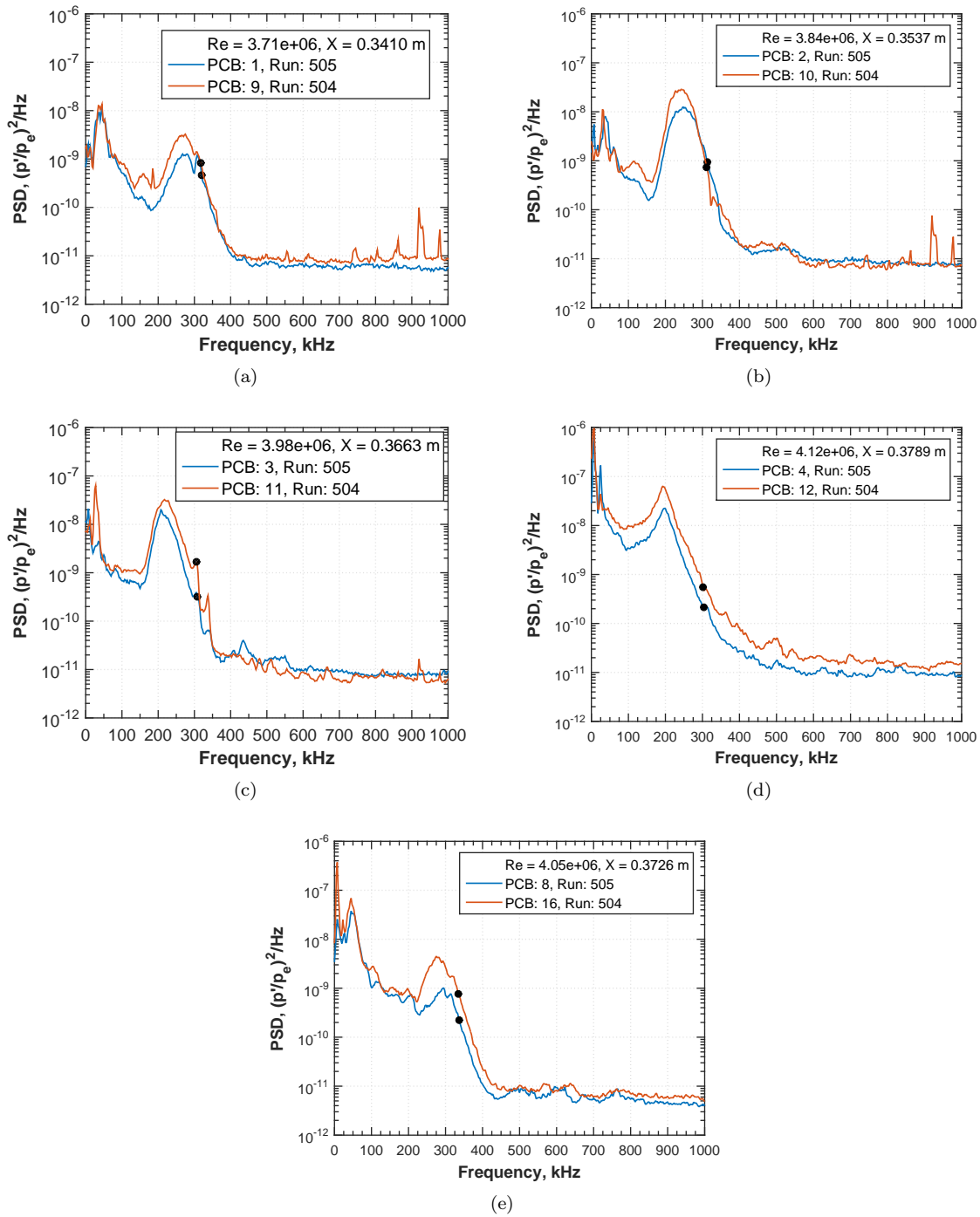
Figure 4. Comparisons between sensors 12° apart, rotated to measure at the same azimuthal angle. The filled circles are the estimated type-II secondary instability frequency.[9]

Table 1. Initial conditions from Runs 504 and 505.

Run	$p_{0,i}$ [psia]	$T_{0,i}$ [C]
504	149.4	155.9
505	150.2	159.1

In general, the two sets of PCB measurements compare well, indicating any changes caused by the rotation do not have a strong effect on the growth of the secondary instability. However, all of the measurements in Run 505 are at a lower power than their counterparts in Run 504. The reason for this is unclear but it could be due to uncertainties in the Reynolds number, which was calculated from the recorded initial stagnation pressure and temperature, and the assumed test Mach number of $M = 6$. The viscosity is calculated from Sutherland's law.

C.   Preliminary Rotation Data

With rotational repeatability established, the new cone was used to examine the spatial extent of the secondary instabilities. In a series of mapping runs, measurements were made every degree over a 10° azimuthal range. Experimental data from Ward[12] shows two instabilities: a high frequency instability over 2.5°-3.5° of azimuth and a low frequency instability over at least 1.5°. The new rotating cone allows investigation of this phenomenon with higher azimuthal resolution and more confidence that the instability measured in each run is the same.

1.   PCB Measurements

Figure 5 shows the power spectra of PCB 3 as it is rotated from 133° to 142°. Initially, there is a low frequency instability whose peak power appears to be unchanged by rotation, as shown in Figure 5(a). However, though the power doesn't change much, the peak frequency shifts higher by 50 kHz over the 2° span. As the sensor is rotated more leeward, the higher-frequency instability grows dramatically over the next 4°, illustrated in Figure 5(b). The peak power increases more than an order of magnitude, and the peak frequency continues to shift upward. Meanwhile, the lower-frequency instability has decreased in power. At 139° the instability appears to have its peak power. Further rotation, shown in Figure 5(c), results in decreasing power at the high frequency. However, the low frequency band increases in power simultaneously.

Because the high and low frequency bands are maximum in different locations they may be two separate instabilities. From these data, it appears that the high frequency instability has a spatial extent of at least 7°, double that of Ward.[12] The Ward instability was measured at a different azimuthal location, about 120°, which may account for some of the difference. Additionally, Ward's roughness was fixed relative to the cone. The cumulative affect of rotating both the sensor and the stationary-wave-generating roughness might have caused the stationary wave under investigation to shift leeward by more than intended rotation, reducing the apparent width of the secondary instability.

The spatial variations of the secondary instability can be observed on more than one sensor. Figure 6 illustrates the same effect on four other sensors. Especially interesting is Figure 6(a) at 139°. At this angle, the PCB measures two distinct peaks at roughly the same power. However, upon further rotation the higher frequency peak disappears.

The data can generally be divided into two bands: a low-frequency band from 100 - 175 kHz, and a high-frequency band from 175 - 325 kHz. Examining two PCBs at the same axial location as they are rotated leeward (Figures 5 and 6(d)), the amplitudes of the fluctuations in each band can be compared. Figure 7 shows these amplitudes compared to the average TSP-inferred heat transfer about 3 mm upstream of the relevant PCBs (discussed in more detail in Section 2). The vortex amplitudes are assumed to change negligibly over the axial distance from the azimuthal slice to the PCB. Note that without computations, it is difficult to detail the relationship between the hot streaks on the TSP and the positions of the actual stationary waves.
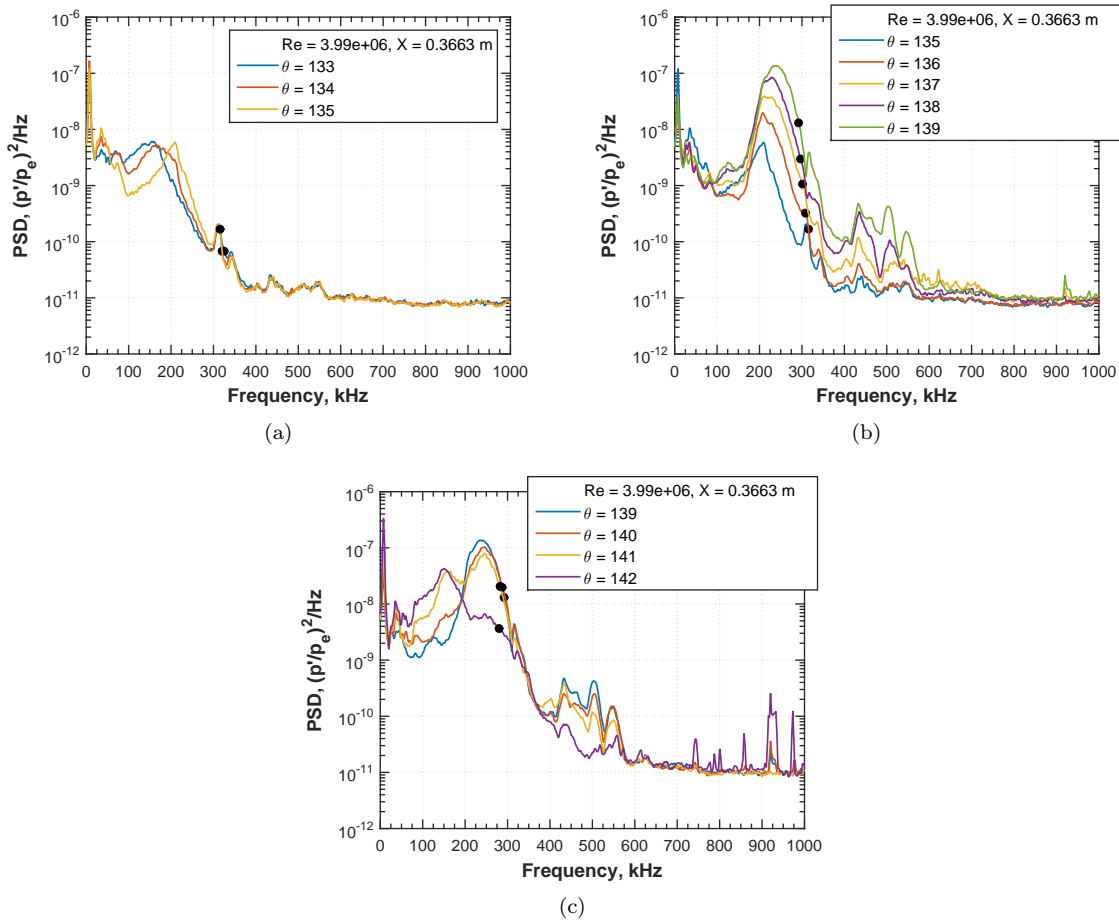
7

(a)

(b)

(c)

Figure 5. Series of PCB power spectra as the sensors are rotated toward the lee ray.

The type-II (higher) frequencies are concentrated under the peak heating areas of the streak, whereas the type-I (lower) frequencies concentrate under the lower-heating troughs. This is especially true for the PCB 11 data. The high frequency data from PCB 3 appear to be concentrated more on the leeward side of a heating peak. If these instabilities are trapped second-modes which scale inversely with boundary-layer thickness, as suggested by Moyes et al.,[8] the higher frequency instability would be under the thin trough of the stationary vortex. More computations are necessary to understand the spatial extent of the various secondary instabilities under these conditions. Future tests will close the gap between 130° and 133°, and measure both higher and lower azimuthal angles.

The amplitudes measured by each PCB can be interpolated to provide an axial-azimuthal map of the location of each band. The PCBs are usually spaced 6.4 mm apart axially and there is data every degree of azimuth. At 119-120°, 125-126°, 130-131°, and 137° there are 12.7 mm between successive axial points. Figure 8 provides the interpolated amplitude maps for both frequency bands. The dashed lines are the approximate experimental trajectories of the heat-transfer streaks. Note that in Fig. 8(a) the amplitude scale is about half that of Fig. 8(b).

The regions of high amplitude for both bands are roughly aligned with the vortex trajectories, supporting that the measured disturbances are secondary instabilities. It is also apparent that the regions of high type-II amplitude correlate with regions of low type-I amplitude and vice versa. The type-II instabilities seem to follow the near-center of the vortex while the type-I is concentrated in between the vortices, as expected
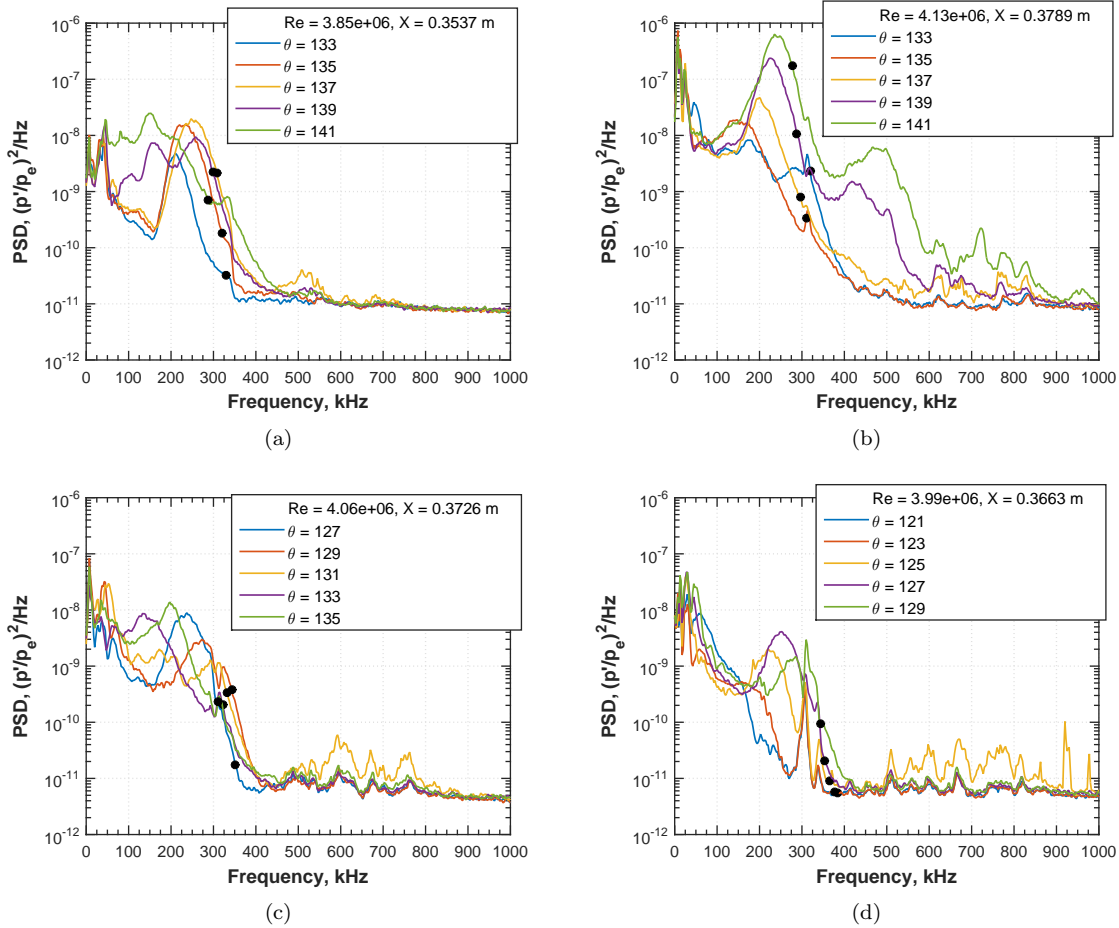
8

Figure 6. Data from four additional sensors that shows the secondary instability change with azimuthal angle.

from low speed flow.

Another interesting property of these instabilities is the change in frequency with rotation. The boundary layer on the cone thickens toward the lee ray. If the instability frequency is inversely proportional to the boundary layer thickness, as expected, then the peak frequency of the measured instability should decrease with increasing azimuthal angle. However, in most of the cases shown in Figures 5 and 6, the frequency increases with increasing azimuthal angle.

This is true with the exception of Figure 6(a) and (c). In these cases, the peak frequency initially rises but at some point a second instability at roughly half the frequency suddenly appears. With further rotation, this second instability also increases in frequency. This rapid change in frequency is another indication that two separate secondary instabilities were observed.

The counterintuitive behavior of the instability frequency may be the result of the stationary crossflow vortices. At high Reynolds numbers, the vortices strongly modulate the boundary layer thickness locally, though on average the boundary layer still thickens toward the lee ray. The local boundary layer thickness changes would have a strong effect on the secondary instability frequencies, though on average the peak frequencies should decrease with increasing azimuthal angle.

As expected, a local increase but an average decrease in frequency is observed using data from two sensors at the same axial location (Figures 5 and 6(d)). The measured peak frequency with respect to azimuthal angle is provided in Figure 9. Computations and a wider experimental azimuthal range are necessary to
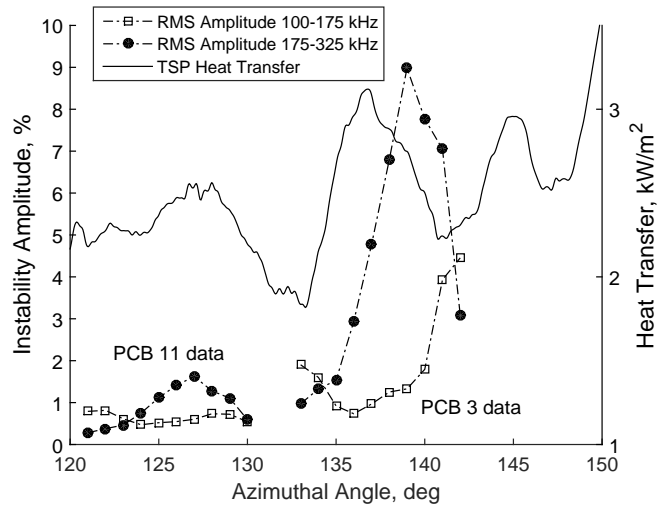
9

Figure 7. A comparison of the RMS amplitude of the secondary instabilities and the calculated heat transfer from TSP. Note there is data from two sensors included. $Re = 3.98 \times 10^6$ **(based on the axial location of the PCBs used).**
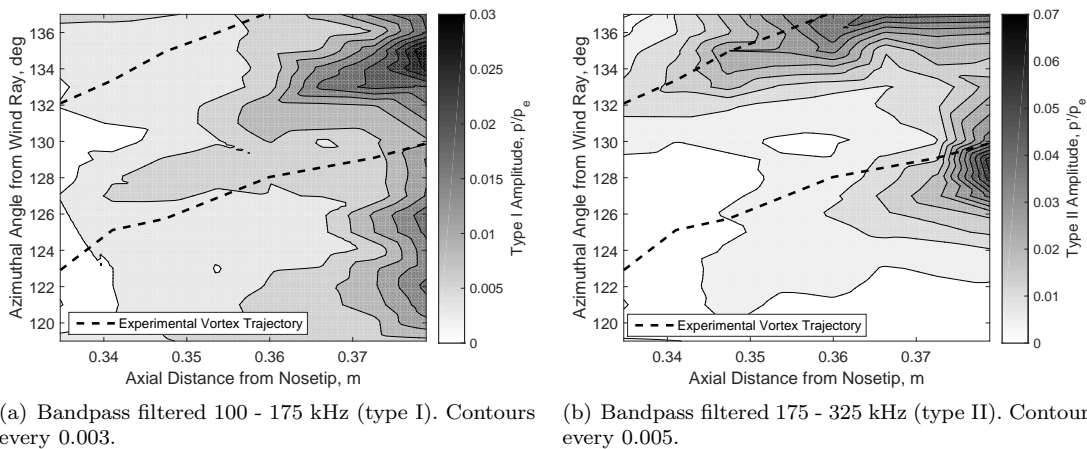

(a) Bandpass filtered 100 - 175 kHz (type I). Contours every 0.003.

(b) Bandpass filtered 175 - 325 kHz (type II). Contours every 0.005.

Figure 8. Contour plots of the interpolated pressure amplitude data collected in the mapping runs.

better understand the relationship between the local boundary layer thickness and the secondary instability frequency.

2. TSP Measurements

Figure 10 shows the heat transfer data from all 10 runs used to collect the rotation data. Note that while these 10 runs were sequential, they were not ordered from lowest azimuthal rotation to highest. Azimuthal slices of the heat transfer data were taken at 0.3636 m axially from the nosetip and a unit Reynolds number $Re_\infty = 10.9 \times 10^6$ /m. Each slice is actually an average of 6 slices over about 1 mm axially. Figure 10(b) shows the mean heat transfer of all 10 slices, with the lower and upper standard deviation.

From figure 10(a), it is clear that small features of the heat transfer are not repeatable. This may be because the vortices themselves have small changes every run, or because of inaccuracies in the TSP data
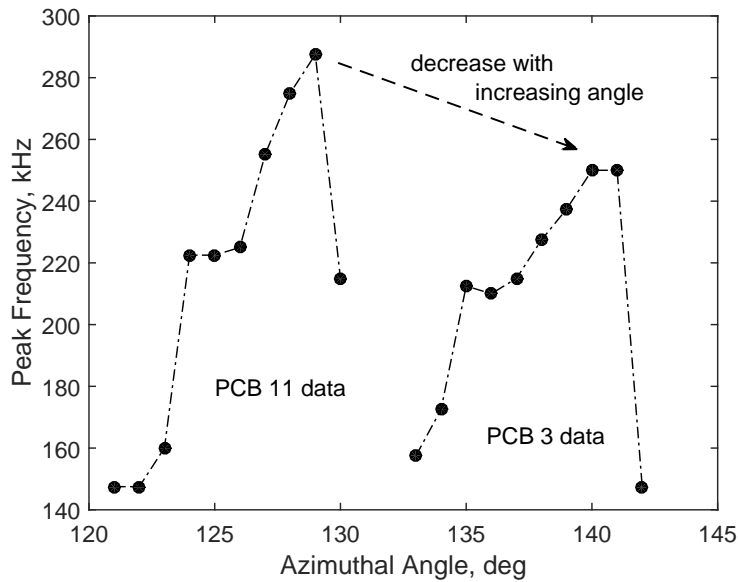
10

Figure 9. Measured secondary instability peak frequency from two sensors. $Re = 3.99 \times 10^6$.

collection and reduction. Regardless, the large structures are fairly consistent. In all the runs there are four large peaks in heat transfer at roughly the same locations, indicative of four stationary vortices (though as discussed in Section 1 the relationship between heating peaks and vortex locations is unclear). One run has a much higher heat-transfer level than the others. This is likely because this data was taken from early on in the run, and residual start-up effects are still present.

(a) TSP-inferred heat transfer from the 10 mapping runs.

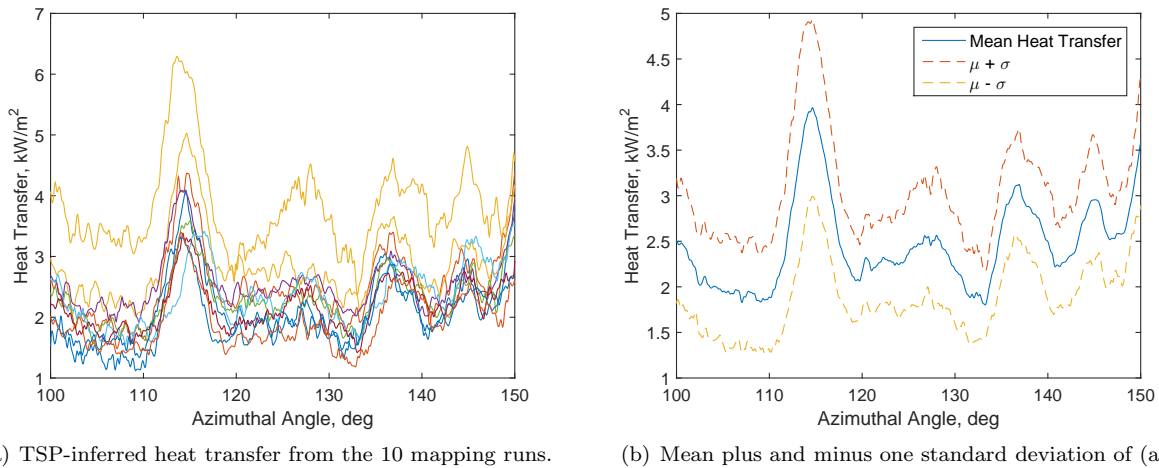(b) Mean plus and minus one standard deviation of (a).

Figure 10. TSP-inferred heat transfer measurements at 0.3636 m from the nosetip for runs at 10 different azimuthal angles. The azimuthal angle is measured from the windward ray.

11

D.   Long-Term Repeatability

One of the primary goals of the present experiment is to establish repeatability of the secondary instabilities so their properties can be studied in depth. Significant progress as been made in this regard. Figure 11 shows power spectra and coherence from two runs, each using the same roughness element. There was no way to put the roughness insert at the exact same orientation for both runs, so the position of the individual elements was different. The difference in roughness position may account for the difference in azimuthal angle at which these measurements were made (132° for the first run and 136° for the second).

   The first run, Run 123, was conducted in June 2015. The second, Run 505, was conducted in February 2016. Each run used a different model. PCB 1 in Run 123 and PCB 2 in Run 505 are the same sensor, but the others are different serial numbers. The data from Run 123 was taken at 132° from the windward ray and at 0.37 m (Figure 11(a)) and 0.38 m (Figure 11(b)). The data from Run 505 was at 136° and 0.34 m (Figure 11(a)) and 0.35 m (Figure 11(b)). Note that the azimuthal angle accuracy is much better for the more recent run (±0.5° in Run 505, ±2.5° in Run 123). The Reynolds number based on the axial position of the PCB is the same for both PCBs in Figure 11(a) and for 11(b).
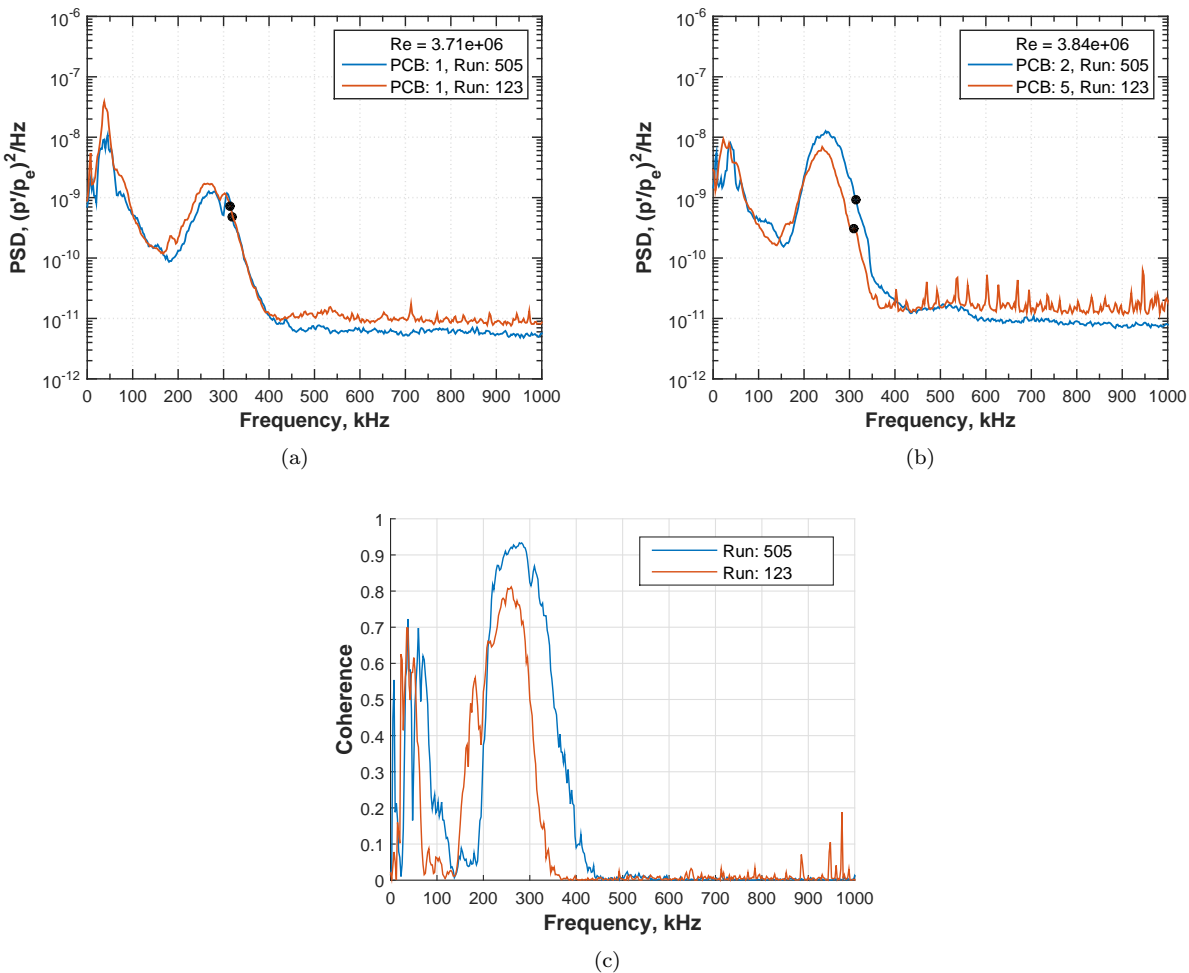

(a)

(b)

(c)

Figure 11.   Power spectra and coherence of secondary instabilities from two runs, 8 months apart. Only the roughness insert is the same for the two runs.

   The upstream sensor power spectra (Figure 11(a)) match quite closely. The peak frequency in Run 123 is

slightly lower than in Run 505. The discrepancy in power levels might be due to inexact PCB calibrations.[13] The downstream sensor pair (Figure 11(b)) are more different, but still match well. Here the peak frequency is also slightly lower in Run 123. The coherence is quite different, with much higher and broader coherence in the more recent run. The measured azimuthal angles of each run differ by 4°, less than the width of the stationary vortex. Given the data from Section 1, measuring a different part of the streak can result in larger power levels and higher peak frequencies. This could account for some of the difference between the two data sets.

## E.   Persistence of Hot Streaks in Turbulent Flow

Figures 12 and 13 show two cases (of at least seven) during which streaks in the TSP persist through transition and into turbulence. Figure 12(a) shows the power spectra from the upstream row of PCB sensors. The colored circles are the type-II frequency estimate. PCB 1, which is at the highest azimuthal angle of 141° from the windward ray, shows a turbulent spectrum. It is expected that if the flow is turbulent at PCB 1, then at the same axial location it will also be turbulent at higher azimuthal angles.

Figure 12(b) provides a TSP temperature-change image from the same conditions as 12(a). The heat-transfer calculation could not be performed for this run because of issues with the thermocouple data. The hot streaks in the TSP, a feature of the stationary crossflow vortices, persist well beyond the axial location of PCB 1, where the boundary layer is turbulent as measured by the pressure sensor. Because the sensors are so close the aft end of the model, it is impossible to determine if the streaks would continue to be present for much longer.

Figure 13(a) shows power spectra from the upstream row of PCB sensors for a different run, this one much closer to the lee ray. In this case, the spectrum at the highest-azimuthal sensor (PCB 1 at 175°) may not be turbulent. However, close to the lee ray the crossflow instability is likely not dominant. Further windward, near 160°, the boundary layer appears turbulent over the sensors. Figure 13(b) provides the TSP temperature-change image from this case. Again, streaks are obvious well into the turbulent region. They are especially noticeable on the opposite side of the lee ray, where there are no sensors to interfere with the TSP measurement.
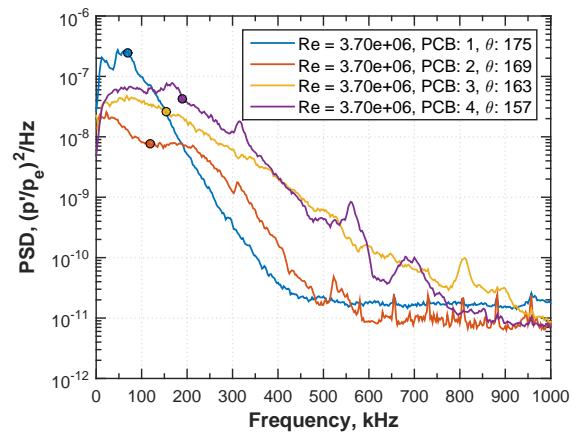
13
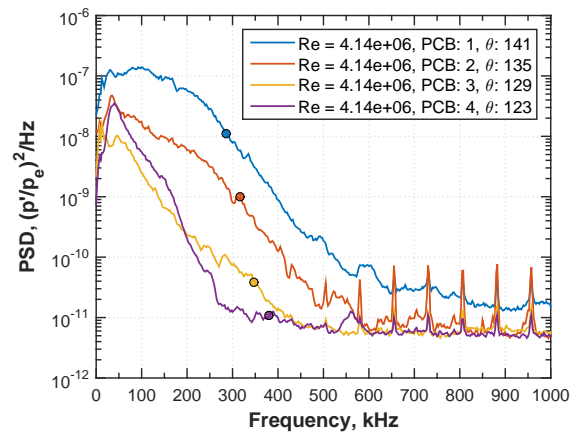
(a) Power spectra from PCB 1-4 (the upstream row) showing turbulent flow at PCB 1.
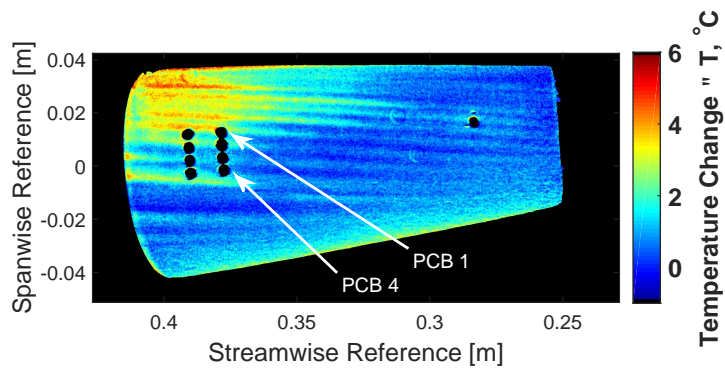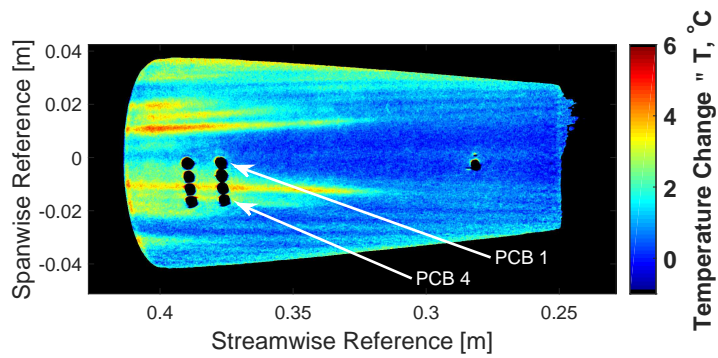

(b) TSP image showing streaks persisting at higher azimuthal angles than PCB 1.

Figure 12.

14

(a)

(b)

Figure 13.

III.   Measurements with 30°Half-Angle Cone Probe

A.   Model and Instrumentation

Measurements of pressure fluctuations were made in the BAM6QT using a 30° half-angle cone model based on a design used at the hypersonic Ludweig tube at the Technische Universität Braunschweig (HLB). The cone geometry was chosen based on the observations of Balakumar who investigated the transfer of freestream fluctuations across the shock to the surface of a cone.[14] The large cone half-angle was selected to allow for enough space for multiple sensors near the nose tip of the model.[15] The model used in the BAM6QT was
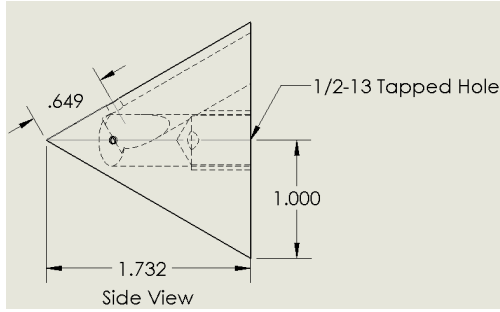
(a) Drawing of 30° half-angle cone.
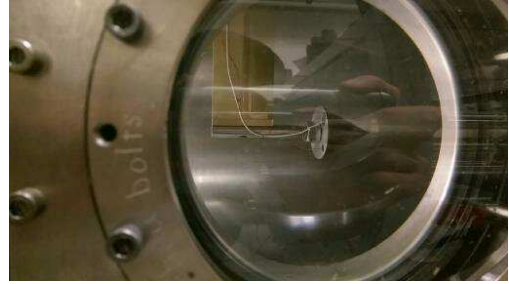
(b) 30° half-angle cone installed in BAM6QT.

Figure 14. 30° half-angle cone used in the BAM6QT.

a 55% scaled model of the cone probe used in the HLB. The cone was scaled to accommodate the smaller diameter test section of the BAM6QT. It is a right circular cone with a 30° half-angle, a 2-inch base diameter, a total length of 1.732 inches, and a nominally sharp nose tip. See Figure 14(a) for schematic of the 30° half-angle cone used in the BAM6QT. The cone was installed in the tunnel using a brass double-wedge support structure as seen in Figure 14(b). The cone was outfitted with a Kulite XCQ-062-15A pressure transducer and a PCB 132A31 pressure transducer located at an axial distance of 0.562 inches downstream of the nosetip, flush mounted to the surface of the cone. These sensors were used simultaneously to measure the cone surface pressure fluctuations. The sensors were offset by 90°.

Two entries were performed using this cone probe: one in November 2015 and another in December 2015. Data were taken for both noisy and quiet flow conditions. After the first entry it was discovered that ground loops between the sensor and the cone caused significant electronic noise that dominated the lower amplitude pressure fluctuations present during quiet flow conditions, however, this noise did not effect the measurements during noisy flow conditions. Therefore, all noisy flow data presented was collected during the first entry with an elevated pre-run electronic noise measurements. In order to remedy this for the second tunnel entry the PCB sensor head was wrapped in electrical tape before installing the sensor on the cone, causing a significant reduction in pre-run electronic noise measured by the sensor. Thus, all data present during quiet flow conditions is from the second tunnel entry where the pre-run electronic noise was significantly reduced. The goal of using the 30° half-angle cone model was to compare the results obtained in the BAM6QT with the HLB using a probe of similar geometry. Additionally, data from the cone probe was generated with quiet flow conditions to compare with data from noisy flow conditions.

B.   Noisy Flow

The HLB facility is a conventional-noise wind tunnel with RMS pressure fluctuations ("noise levels") at typical model locations ranging from 1.0% to 1.6% and a test-section Mach number of approximately $M = 5.9$ as measured by pitot probes[15,16] . When run in conventional-noise mode with bleeds closed the BAM6QT maintains RMS pressure fluctuations of 1.5 - 4.5%, with a test section Mach number of between $M = 5.6$ to 5.9.[17] Thus, run conditions between the two facilities are similar.

16

Five runs were made in the BAM6QT with unit Reynolds numbers ranging from $Re = 6.1{\times}10^6$/m to $Re = 11.0{\times}10^6$/m under noisy flow conditions. The cone probe was located along the centerline of the tunnel with the probe support located as far downstream as possible from the throat at $z = 94.0$ in. Figure 15 shows the PSD of the normalized pressure fluctuations as measured by the PCB in both the BAM6QT and HLB facilities. The mean pressures were measured using the Kulite XCQ-062-15A sensor that was installed on the model at the same distance from the nosetip and offset $90°$ azimuthally from the PCB.
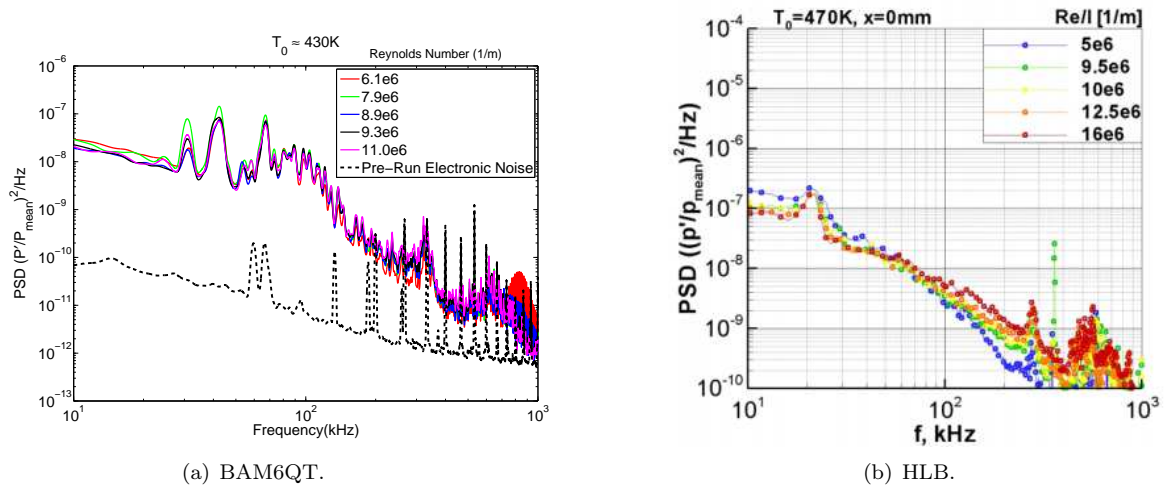

(a) BAM6QT. (b) HLB.

Figure 15. PSD of normalized pressure fluctuations measured by the PCB on the $30°$ half angle cone model in noisy flow with varying unit Reynolds Number. HLB results taken from Ali et al.[15]

Figure 15(a) exhibits a unit-Reynolds number effect similar to that shown in 15(b). This is an expected effect that occurs in high speed wind tunnel facilities that correlates with sound waves emitted from the turbulent boundary layer on the nozzle walls. These sound waves propagate throughout the nozzle and are quantified as an increase in the RMS value of pressure fluctuations. The results differ greatly for lower frequencies between the two facilities. The PSD generated in the BAM6QT facility shows three distinct low frequency peaks present for all Reynolds Numbers at approximately 30, 43, and 68 kHz with these peaks most prominent when $Re = 7.9{\times}10^6$/m , whereas the PSDs from the HLB facility only show one low-frequency peak at approximately 20 kHz. Additionally, the amplitude of the PSD at 10 kHz is nearly an order of magnitude higher at the HLB facility when compared to the BAM6QT. The reason for the discrepancies between the two facilities is not yet known.

Figure 16 shows the PSD of surface pressure fluctuations from both the PCB and Kulite pressure transducer sensors for a range of Reynolds Numbers. For this particular Kulite the resonant frequency is 326 kHz so the sensor should have a flat dynamic response up to about 98 - 130 kHz (30% - 40% of the resonance frequency for an A-screen Kulite).[18] The PCB has a low frequency cut off of 11 kHz, and so the two sensors have a frequency response that should overlap between approximately 11 and 130 kHz. The dash-dotted lines represent the PSDs generated by the Kulites and the solid lines represent the PSDs generated by the PCB sensors, with the colors matching for sensor data from the same Reynolds number conditions. For all Reynolds numbers the PCBs are in good agreement with the Kulites up to approximately 15 kHz. However, the PCBs exhibit an elevated spectra when compared to the Kulites for 15-130 kHz overlap region between the sensors.

This behavior matches the results of Casper et al. which showed that at higher Reynolds Numbers when Kulite and PCB sensors were under a transitional or fully turbulent boundary layer the PCB measured elevated spectra.[19] It was postulated that this discrepancy could be caused by asymmetric transition over the cone thus causing the sensors to measure two different parts of the transition region. However, based on the work by Stainback, it is unlikely that this is the case for the present experiments since the local,
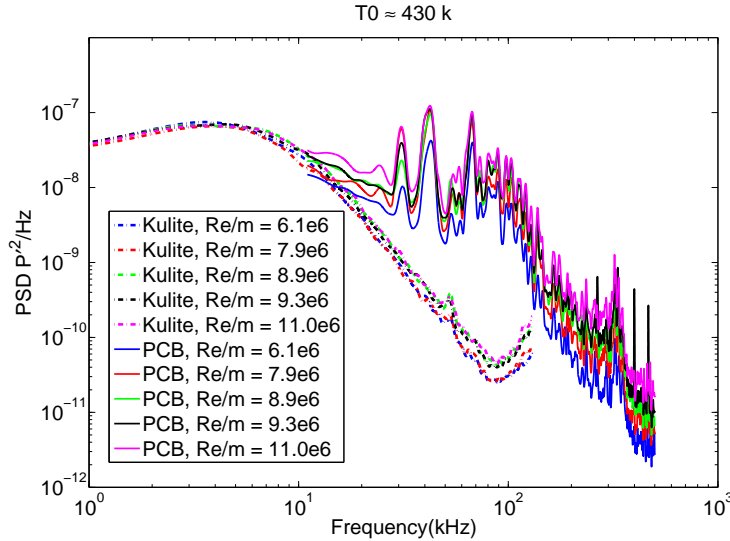
17

Figure 16. PSD of surface pressure fluctuation measurements with both PCB and Kulite pressure sensors during noisy flow.

slant-height based Reynolds number is approximately an order of magnitude less than the freestream unit Reynolds number, thus making boundary layer transition unlikely to occur.[20] The reason for the discrepancy between the sensors remains unknown. It is known that the measurements from piezoelectric sensors, such as the PCBs used in this experiment, are sensitive to acceleration whereas the measurements from the Kulites, which utilize a wheatstone bridge circuit to measure pressure, are not expected to be sensitive to vibrations.[13] Therefore, the discrepancy could be caused by vibrations from the model or support structures contaminating the pressure fluctuations measured by the PCB, however, further testing is required to determine the exact cause of the discrepancy.

Figure 17 shows the RMS of the surface pressure fluctuations, normalized by the surface pressure, as measured by both the PCB and Kulite sensors for a range of Reynolds numbers during noisy flow conditions. This measurement is commonly referred to as the noise level of a facility. The Kulite data were integrated from 3-45 kHz and the PCB data were integrated from 11-45 kHz. The noise levels measured by both sensors range from 2.05 to 3.57 % decreasing in general as the Reynolds number increases. This matches the Reynolds number dependence seen at the HLB facility, however the surface-pressure noise levels measured in the BAM6QT are approximately double those at the HLB tunnel. This could be caused by a multitude of differences between the two facilities as well as the different size of the cone probe used in the BAM6QT. The sensors on the cone in the BAM6QT could also be measuring a different regime of transition thus causing the elevated noise levels, however further testing would be required to determine the exact cause of the noise level discrepancy. Additionally the noise levels measured by the cone probe in the BAM6QT are lower than those measured previously using pitot probes for the same flow conditions.[17] This difference matches what was observed in the HLB facility and is obviously caused by the different transmissions of disturbances through the shock and shock layer of the cone.[15]
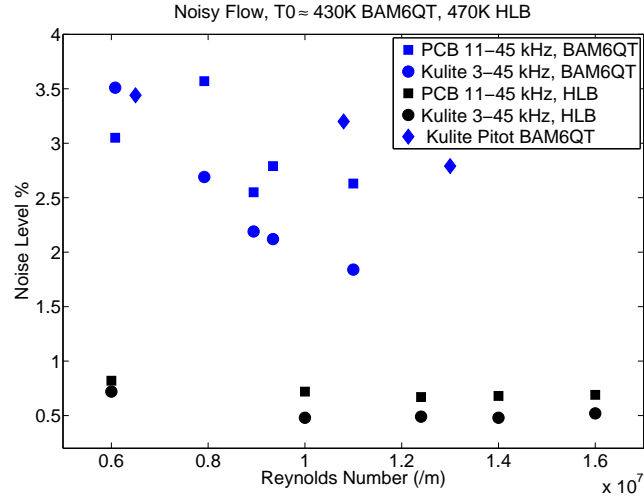
18

Figure 17. RMS of cone surface pressure fluctuations normalized by mean surface pressure.

C. Quiet Flow

Eight runs were made in the BAM6QT with unit Reynolds numbers ranging from $Re = 5.7 \times 10^6$/m to $Re = 12.6 \times 10^6$/m under quiet flow conditions. Figure 18 shows the PSD of the pressure fluctuations, normalized by the mean surface pressure, as measured by the PCB. The mean surface pressures were measured using the Kulite sensor installed on the model at the same distance from the nosetip and offset $90°$ azimuthally from the PCB. Due to an error in oscilloscope sampling rate settings, PSD and RMS pressure fluctuation measurements from the Kulite are only available for two runs from which the PCB data is unusable due to elevated electronic noise levels.
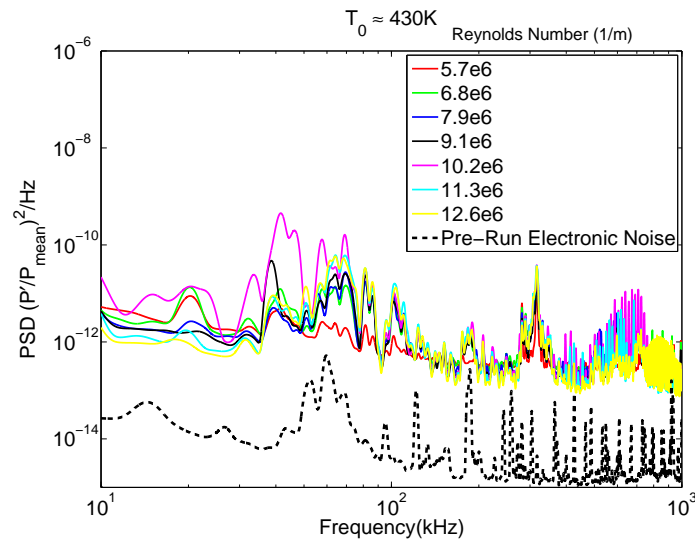

Figure 18. PSD of cone surface pressure fluctuations normalized by mean surface pressure during quiet flow.

Figure 18 exhibits a unit-Reynolds umber effect similar what is shown in Figure 15. As expected the power of the pressure fluctuations for quiet flow are much smaller, by approximately three orders of magnitude,

19

when compared to the pressure fluctuations from noisy flow. The PSD for quiet flow has low-frequency peaks similar to those shown for the noisy flow conditions, however the peaks do not exist for all Reynolds Number and they are not nearly as pronounced. The peaks are most prominent when $Re = 10.2 \times 10^6/\text{m}$ where three peaks appear at approximately 42, 57, and 98 kHz. Also note that the pre-run electronic noise measured is significantly lowered during quiet flow conditions present in the second entry for reasons discussed in Section A.

Figure 19 shows the PSD of surface pressure fluctuations from both the PCB and Kulite pressure transducer sensors for a range of Reynolds numbers. The Kulite was the same sensor as used for the noisy flow runs with a resonant frequency of 326 kHz therefore the sensor should have a flat dynamic response up to about 98 - 130 kHz and the two sensors should have the same overlap of approximately 11 to 130 kHz. Once again for the PCBs have elevated spectra when compared to the Kulites throughout the 15-130 kHz overlap region, however for the quiet flow conditions it appears that the PCBs also measure elevated spectra in the 11-15 kHz range.
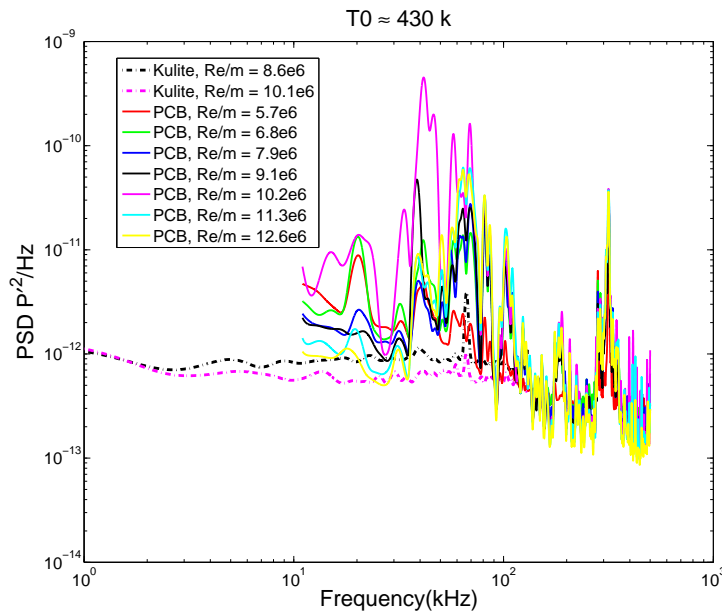

Figure 19. PSD of surface pressure fluctuation measurements with both PCB and Kulite pressure sensors during quiet flow.

Figure 20 shows the noise levels of the surface pressure fluctuations, normalized by the surface pressure, as measured by the PCB and Kulite during quiet flow conditions for varying Reynolds Numbers. The noise levels measured by both sensors ranges from 0.01% to 0.04% There is good agreement between the noise levels measured by both sensors and with the noise levels measured by the Kulities and PCBs using pitot probes. Unlike the noise levels measured during noisy flow conditions there does not appear to be a downward trend of noise levels with increasing Reynolds numbers, instead the noise levels remain relatively constant.
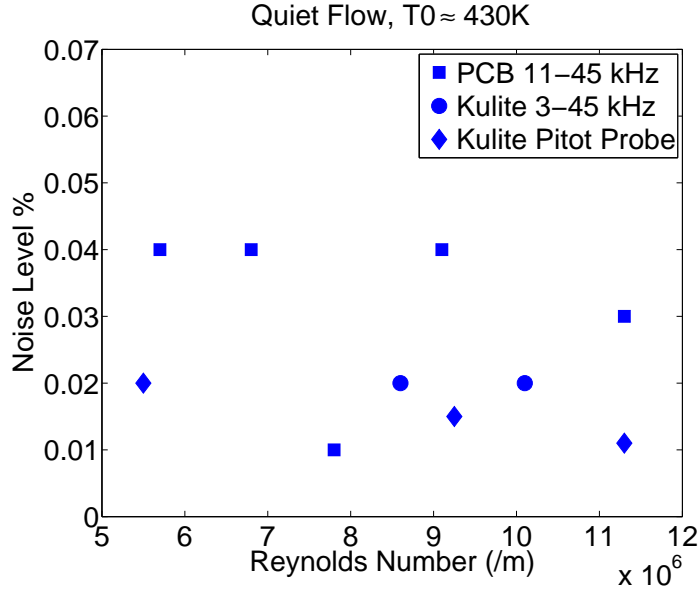
Figure 20. **Noise levels of cone surface pressure fluctuations normalized by mean surface pressure during quiet flow.**

IV.   Transition Measurements on a Flared Cone

In recent years, efforts have been made to help improve the prediction methods used to determine when a boundary layer will begin the laminar-turbulent transition process at hypersonic speeds. Transition at Mach 6 on axisymmetric geometries near zero degrees angle of attack is dominated by the second-mode instability. The second-mode wave is similar to a trapped acoustic wave that reflects between the surface of a model and the sonic line within the boundary layer.[21] The nature of this reflection results in the tuning of the second-mode instability to the boundary-layer thickness. A flared cone model was designed by Wheaton[22] to maintain a boundary layer with a near constant thickness which amplifies a narrow band of second-mode instability frequencies.

A.   Model and Instrumentation

All experiments were performed on a flared cone with a constant 3-meter circular arc. The model consists of a nosetip, a roughness insert, and a frustum. The frustum is shown in Figure 21. This model is referred to as the Roughness Insert Cone. The total model length is 51.7 cm with a base diameter of 11.4 cm (4.5 inches). The nosetip is 25.4 cm long with a nose radius of 152 μm (0.006 inches) and an opening half-angle of approximately 1.5°. The cone was designed with a space 0.635 cm (0.250 inches) wide between the nosetip and the frustum. This gap is filled with a removable roughness insert that can either be left unmodified to test smooth wall cases, or can include roughness elements. A Rod Insertion Method (RIM) roughness is created by drilling holes into the insert surface, inserting a brass rod, and then machining the element down to the desired height.

Sensors are placed along a single ray at a distance of 34.0, 36.5, 39.0, 41.5, 44.1, 46.6, and 49.2 cm from the nosetip. Two azimuthal arrays of PCB sensors have been added at distances of 41.5 and 46.6 cm from the nosetip. Three additional sensor holes at +/- 90° and 180° from the main sensor ray at 46.6 cm from the nosetip are used to facilitate the use of a precision angle-of-attack adapter as was reported in Sweeney et al.[9] The model is currently capable of obtaining data simultaneously from 22 PCB132A31 pressure sensors as well as one Schmidt-Boelter heat transfer gauge. In order to reduce electrical noise, each PCB sensor was wrapped in heat shrink tubing before installation in the model. Additionally, a permanent marker is used to

place black dots spaced 30°apart azimuthally at each sensor station to provide reference points when image processing.
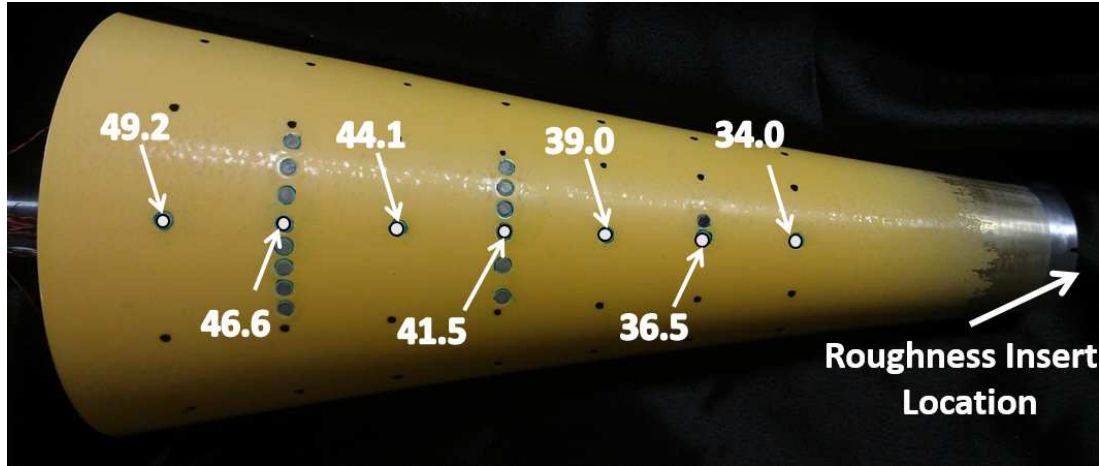

Figure 21. Photograph of the Roughness Insert Cone with a 11.4 cm base diameter and sensor locations noted in distance from the sharp nosetip in centimeters.

B.   Results from a RIM Roughness Insert with 45 Discrete Elements

A new RIM insert with 45 evenly spaced roughness elements was tested. Each roughness element had a diameter of approximately 840 μm and a height of 0.005" (130 μm). The RIM insert was first installed with one of the elements directly upstream from the main sensor ray. Simultaneous comparison of temperature sensitive paint images, power spectral densities, and pressure fluctuation magnitudes show how the heating on the model surface relates to the growth and breakdown of the second-mode instability.

Figure 22 is a temperature sensitive paint (TSP) image of the heating to the model at a $\mathrm{Re} = 9.3 \times 10^6$/m with flow from right to left. The power spectra are shown in Figure 23(a). The RMS pressure fluctuation magnitudes are shown in Figure 23(b). These were computed by integrating over a 200 kHz bandwidth centered at the peak second-mode frequency at 200 discrete intervals over a 2.5 second run time. The TSP image shows the characteristic hot-cold-hot heating pattern similar to what is observed when no roughness is present. Unlike the smooth wall which has approximately 90 streaks that develop at the same downstream location, this pattern has 90 streaks that develop in a staggered pattern. The power spectra for the five upstream PCB sensors indicate a laminar boundary layer with a second-mode wave present. The RMS pressure fluctuations are near 2% at the most upstream sensor. They continue to amplify until they reach their peak between 30-35% of the surface pressure just downstream of the first increase in heating. It should also be noted that the bandwidth of amplified frequencies increases from 100 kHz to 260 kHz between the sensor at 34 cm and the sensor at 44.1 cm. As the stagnation pressure drops over the duration of the run, the first increase in heating moves downstream over this same sensor. As a result, pressure fluctuations increase from 10% to 35% as the center of the first increase in heating moves over the sensor. The PCB sensor at x = 46.6 cm shows broad spectral filling indicative of transition. The TSP image shows that this sensor is at the beginning of the second increase in heating. The power spectra of the sensor at the furthest downstream position shows an almost fully turbulent boundary layer with pressure fluctuations of approximately 3%.
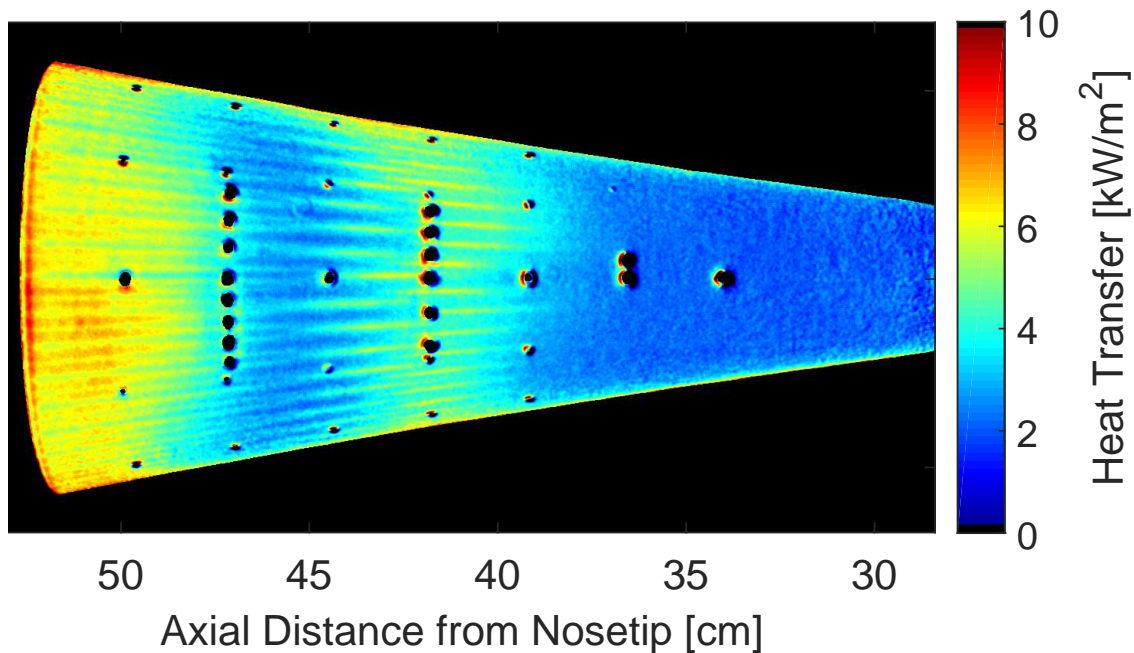
Figure 22. TSP image with RIM insert composed of 45 evenly spaced elements at a unit Re $\approx 9.3 \times 10^6$/m. Flow is from right to left.
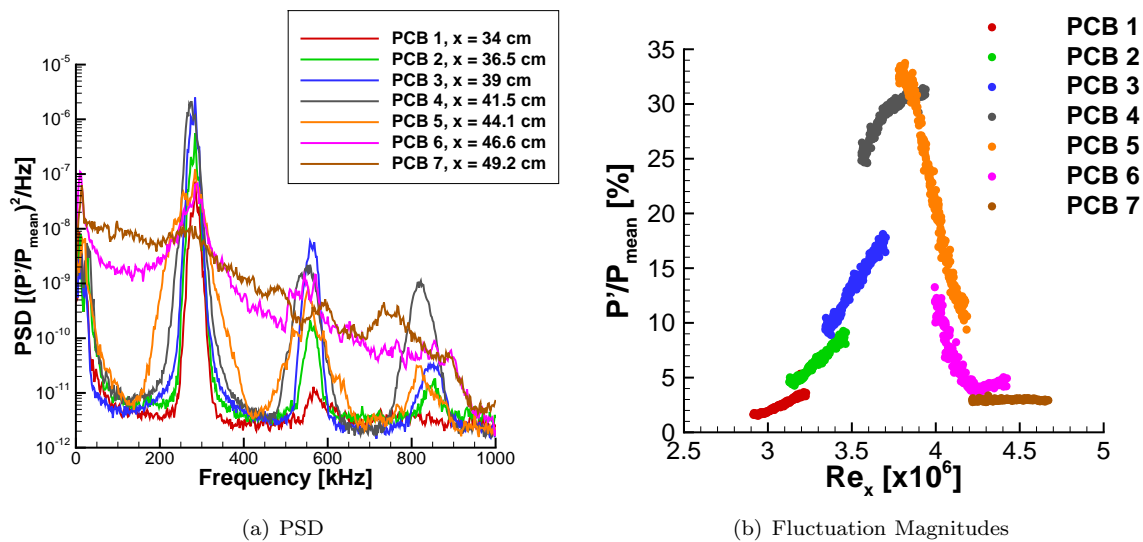

(a) PSD

(b) Fluctuation Magnitudes

Figure 23. PSD of sensors on main ray processed simultaneously with Figure 22 as well as pressure fluctuation magnitudes throughout the duration of the run.

Figure 24 is an enlarged view of Figure 22 near where an azimuthal array of PCB pressure sensors are located. The table provided with the image shows the azimuthal distance of each PCB from the main sensor ray. PCB sensors 4, 11, 12, 13, and 15 are directly downstream from a roughness element while sensor 14 is downstream from the gap between two sensors. The PSDs for all sensors on this array, shown in Figure 25, show a second-mode instability with strong first and second harmonics. Integrating the power spectra

23

between 200 and 400 kHz to obtain the pressure fluctuation magnitude shows that the fluctuations measured by PCB 14 (placed between roughness elements) is 20% lower than the mean of pressure fluctuations measured by sensors directly downstream from a roughness element. The mean pressure fluctuation magnitude for all six sensors is 28%. The RIM insert was then rotated 4°so that sensor 14 was directly downstream from a roughness element while the other PCB sensors were in the space between elements. Pressure fluctuations were computed at a similar unit $Re_\infty \approx 9.3 \times 10^6/\text{m}$. The mean pressure fluctuation magnitude of the six sensors is once again 28%, but the pressure fluctuations measured by PCB 14 now only differ from the mean measurement of the other sensors by 6%. The cause of this has not yet been determined. Future experiments will use PCB sensors with different calibrations to determine if this effect is due to the uncertainties of the PCB sensor calibrations or linked to some physical phenomenon.

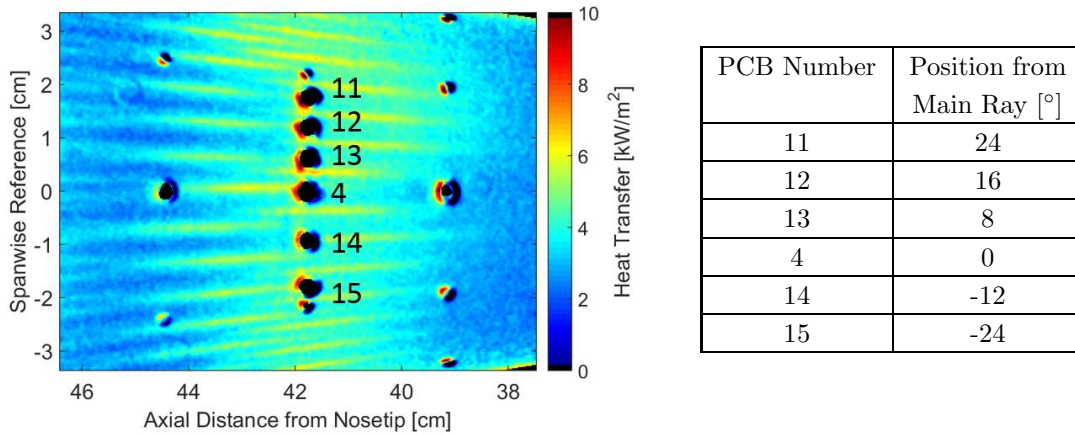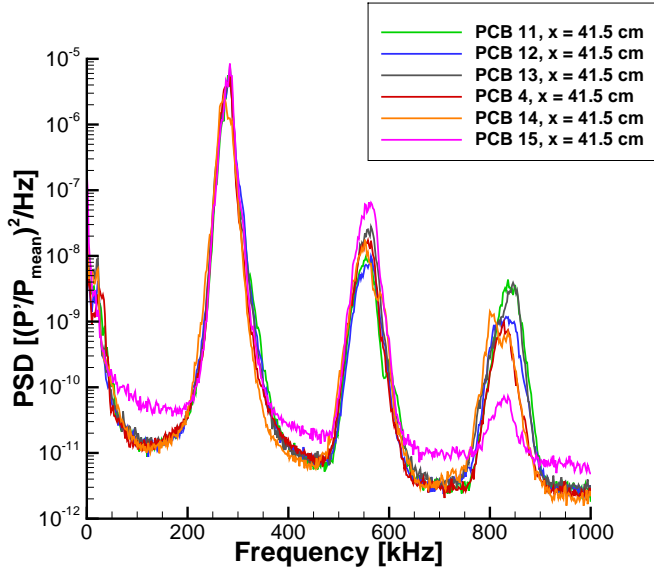| PCB Number	Position from Main Ray [°]
11	24
12	16
13	8
4	0
14	-12
15	-24

Figure 24. Enlarged portion of TSP image in Figure22 with azimuthal array of PCB sensors labeled. The table provides the azimuthal spacing of each sensor from the main sensor ray.

24

PCB Number	P'/P$_{mean}$ [%] Original	P'/P$_{mean}$ [%] RIM Rotated
11	30.6	26.3
12	30.1	27.0
13	29.2	32.2
4	28.0	29.9
14	23.4	26.5
15	32.4	26.8
Mean	29.9	28.1

Figure 25. PSD from the six azimuthally spaced sensor at the same instant as the TSP image in Figure 22 along with a table of pressure fluctuation magnitudes. PSD corresponds to "Original" data in table.

C. Maximum Second-Mode Magnitude – Quiet versus Conventional Facilities

The second-mode instability reaches a maximum pressure fluctuation magnitude as it amplified prior to breakdown. Results compiled by Marineau et al.[23] for various experiments in traditional "noisy" hypersonic facilities show that as the edge Mach number increases, the maximum second-mode amplitude also increases. The "noisy" tunnel data is shown in Figure 26. Two points have been added to the plot based on data taken using the Roughness Insert Cone under quiet conditions in the BAM6QT facility. An edge Mach number of 3.1 was computed for the Roughness Insert cone using STABL. For a single experiment without using roughness (smooth), the maximum pressure fluctuation magnitude was 27.5%. When testing with a RIM insert with 45 roughness elements, the maximum amplitude measured was 34.2%. It can be seen in Figure 26 that there is a discrepancy between data obtained in a quiet tunnel versus conventional facilities. Tests performed with different RIM inserts will produce more data points at an edge Mach number of 3.1. Methods of testing using a perturber to produce second-mode fluctuations on a 7°half-angle and a 3°half-angle straight cone with a sharp nosetip are currently being developed. If successful, testing with these two different cone half-angles will provide data under quiet flow conditions at edge Mach numbers of 5.4 and 5.6, respectively.

D. Future Experiments and Data Processing Techniques

Comparisons to smooth wall cases could not be presented because data were not collected at the proper conditions. Future testing with a smooth wall at a unit Re $\approx 9.3\times10^6$/m will allow for direct comparison between the natural transition observed without roughness and results with roughness. Additionally, experiments are currently being conducted to further understand the relationship between the position of the pressure sensors relative to roughness elements and the effect on second-mode wave growth and breakdown. RIM inserts with 45 roughness elements and heights of 0.010" and 0.015" have been fabricated.

Data processing techniques to investigate second-mode wave packets are also being explored. Since power spectral densities are time averaged, often the fact that second-mode waves form in packets is not fully appreciated. The author is currently investigating if processing via a wavelet analysis coupled with PSD computations on smaller time frames could provide new insight into the growth and breakdown of second-mode wave packets.
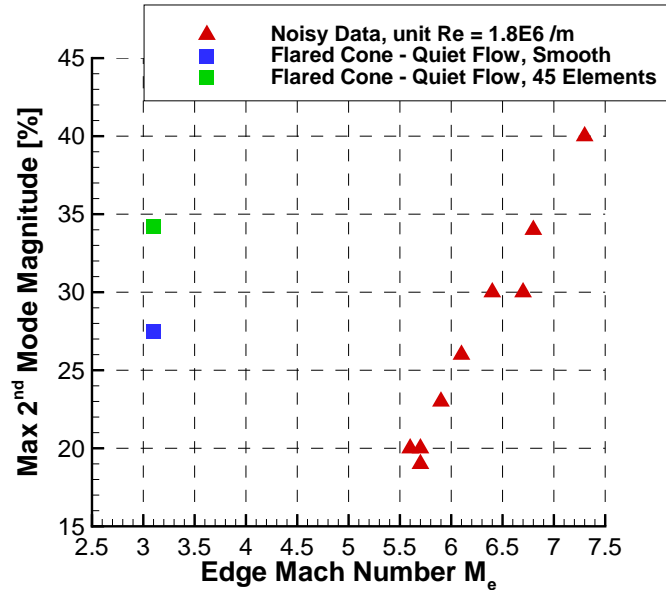
Figure 26. **Comparison of maximum second-mode amplitudes in conventional facilities from Reference 23 versus two measurements under quiet flow in the BAM6QT facility.**

V.   Transition measurements through a finite span compression corner

Boundary layer flow approaching any ramp or control surface on a hypersonic vehicle is subjected to adverse pressure gradients due to the shock wave present at a compression corner. This adverse pressure gradient will retard the incoming boundary layer and, if strong enough, cause separation. At these locations, laminar-turbulent transition commonly occurs within the free-shear layer and can lead to some of the highest heating loads on the surface.[24] Gaining a basic understanding of how the free-shear layer affects the natural transition on a body will help in designing many maneuverable high speed vehicles.

A.   Model

A variation of the model used by Oberkampf et. al. was designed and fabricated for use within the BAM6QT.[25] The model consists of a 7° half angle cone with a nominally sharp nose tip. At 0.7L, where L is the length of the model, a slice was machined into the cone. This slice is parallel with the model's axis and provides the upstream surface of the compression corner. Three interchangeable ramps are 0.038m long and allow deflection angles of 10°, 20°, and 30°. These ramps span the width of the slice.

Thirteen PCB132A31 fast pressure sensors were used to measure pressure fluctuations on the surface of the model. Nine sensors were placed on the centerline of the slice. Six of these sensors were positioned on the slice of the model and then three were placed on the ramps. The sensors begin at an axial distance of 0.306m from the nose tip and are spaced at 0.013m intervals. Four PCB's were placed around the azimuth upstream of the slice to ensure the tests were conducted at 0.00° angle of attack. Additionally, one Schmidt-Boelter heat transfer gauge was placed upstream of the slice, on the centerline, to calibrate the TSP images. An image of the model can be seen in figure 27.

B.   Current Results

Preliminary results have shown the importance of freestream noise to the flow through a compression corner. Measurements made with the 10° and 20° ramps did not show any heating increase that could be inferred as
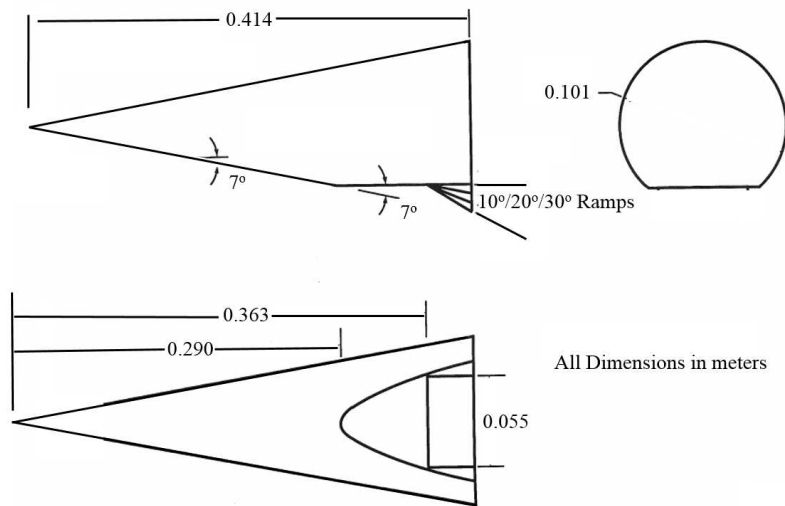
26

Figure 27. Schematic of the model with dimensions in meters. Redrawn from Reference [25]

reattachment and are not included in the current section. However, with the $30°$ ramp the flow did reattach on the model.

Figure 28 shows the surface heat transfer for both quiet and noisy flow at Re $= 12.4 \times 10^6$/m. In the quiet flow image, the slice portion of the model does not show any change in heating that could be associated with separation. Thus, the separation point is not yet known. Further downstream on the ramp a clear reattachment line can be seen near the aft end of the ramp. Reattachment is three-dimensional and slightly asymmetric and produces over twice the heating present for the noisy case. The bottom half of figure 28 shows the same Reynolds number but for noisy flow. The predominant difference in noisy flow is the lack of a large clear separated region on the ramp and the associated reduction in heat transfer on the surface. Investigation of sensors upstream of the slice show that the boundary layer has transitioned before the slice in the noisy flow case.

Figure 29 shows the spectra for the three sensors immediately upstream of the ramp and the three sensors on the ramp. The upstream sensors are peaky and discernible features are difficult to spot. As the axial distance increase the spectra smooth out and begin to transition at x = 0.403m. This sensor lies immediately upstream of the reattachment point. This situation suggests that the boundary layer has transitioned off the surface of the model and is reattaching turbulent. Figure 30 shows the spectra for the noisy flow case. The two furthest downstream sensors were damaged during this run and are omitted the plot. The spectra are much smoother and have begun to transition by x = 0.370m downstream. This is prior to the ramp.

Based on this information, it seems possible to measure shear layer transition in both quiet and noisy flow within the BAM6QT. Adjustments and more complete measurements are being done to obtain a better picture of the resulting flowfield.
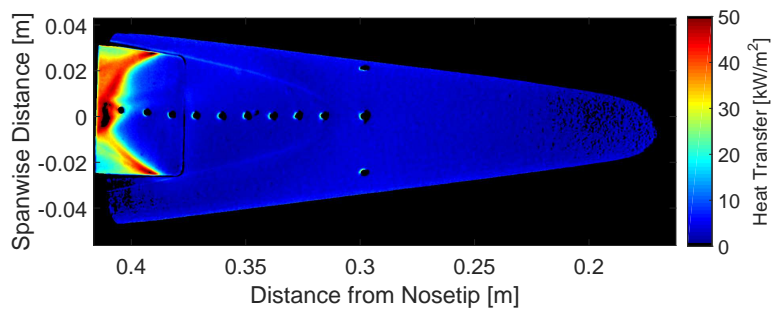
(a) Quiet flow.
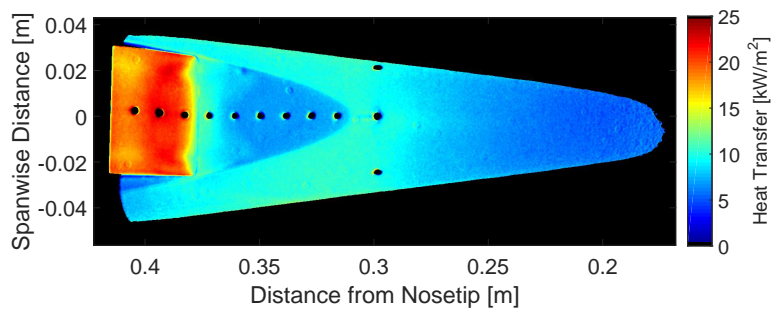
(b) Noisy flow.

Figure 28. TSP of the model at Re $= 12.4 \times 10^6$/m in both quiet and noisy flow.
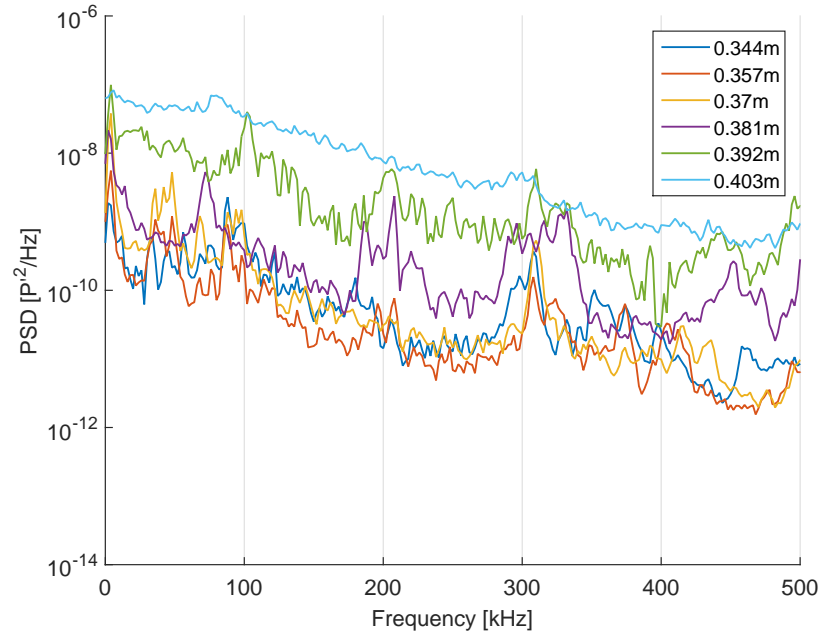
Figure 29. PSD in quiet flow at an Re $= 12.4 \times 10^6$/m. The distances in the legend are measured axially from the model nosetip. Sensors downstream of 0.381m are on the ramp. All others are on the slice.
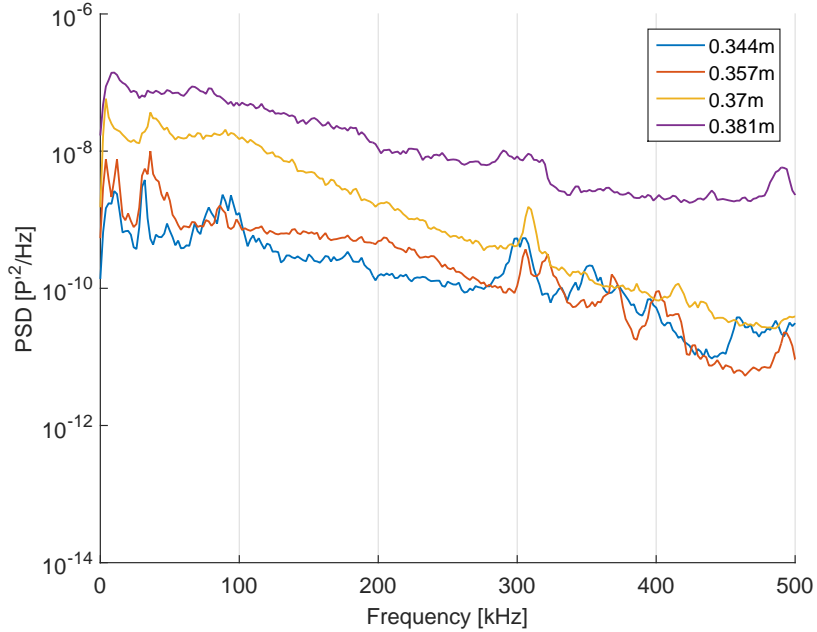
Figure 30. PSD in noisy flow at Re = $12.4{\times}10^6$/m. The distances in the legend are measured axially from the model nosetip. The sensor at 0.381m is on the ramp, all others are on the slice.

VI.   Conclusion

1. A $7°$ half-angle cone at $6°$ angle of attack was used to investigate the growth of secondary instabilities of stationary crossflow waves. A new model allows the rotation of the fast pressure sensors independently of the rest of the cone. First, repeatability of the cone with respect to rotation was established by taking measurements with two different sensors at the same axial and azimuthal location. By rotating the sensors across a stationary vortex, it was found that at least two secondary instabilities seem to exist independently in different areas of the streak. These instabilities are each spatially confined, spanning about $7°$. The frequencies of the instabilities appear to increase locally with increasing azimuthal angle, the opposite of the expected trend. This may be the result of the strong modulation of the local boundary layer thickness by the stationary waves. In addition, long-term repeatability of the secondary instability measurements was shown. Finally, two cases were shown in which the hot streaks in the TSP persisted through transitional and turbulent flow.

2. Using a $30°$ half-angle cone equipped with PCB and Kulite pressure transducers, experiments were performed to measure pressure fluctuations during both bleeds open and closed conditions. Noisy flow results were compared with results generated at the hypersonic Ludwieg tube at the Technische Universitat Braunschweig and it was observed that the low frequency behavior of the pressure fluctuations differed greatly between the two facilities. Additionally, results from the two pressure transducers were compared and it was found that the PCBs measured greater amplitude of pressure fluctuations across the overlap bandwidth.

3. A RIM insert with 45 evenly spaced elements created a new heating pattern when compared to the smooth wall case. The growth and breakdown of the second-mode wave was observed, and peak pressure fluctuations of 35% were measured. Even though the pattern of heating was altered, peak pressure fluctuation magnitudes when testing with RIM inserts were similar to those measured under the smooth wall configuration.

4. Measurements of a cone with a slice and flap were made and separation and reattachment of the boundary layer was observed under quiet flow. Reattachment heating exceeded 50 kW/m^2 in some locations of the ramp for quiet flow as opposed to approximately 20 kW/m^2 in noisy flow. Spectra indicate that the flow begins to transition at the furthest downstream sensor which is immediately upstream of reattachment. This suggests that shear-layer transition might have occurred. A clear separation bubble was not observed for noisy flow. Spectra from noisy flow conditions indicate transition upstream of the slice. This would produce a fuller boundary layer profile and be more resistant to separation.

VII.   Acknowledgements

References

[1]Deyhle, H. and Bippes, H., "Disturbance Growth in an Unstable Three-Dimensional Boundary Layer and Its Dependence on Environmental Conditions," *Journal of Fluid Mechanics*, Vol. 316, 1996, pp. 73–113.

[2]Kohama, Y., Saric, W., and Hoos, J., "A High-Frequency, Secondary Instability of Crossflow Vortices that Leads to Transition," *Proceedings of the Conference on Boundary Layer Transition and Control*, 1991, pp. 4.1–4.13.

[3]Malik, M., Li, F., and Chang, C.-L., "Nonlinear Crossflow Disturbances and Secondary Instabilities in Swept-Wing Boundary Layers," *IUTAM Symposium on Nonlinear Instability and Transition in Three-Dimensional Boundary Layers*, edited by P. W. Duck and P. Hall, 1996, pp. 257–266.

[4]Malik, M., Li, F., Choudhari, M., and Chang, C.-L., "Secondary Instability of Crossflow Vortices and Swept-Wing Boundary-Layer Transition," *Journal of Fluid Mechanics*, Vol. 399, 1999, pp. 85–115.

[5]White, E. and Saric, W., "Secondary Instability of Crossflow Vortices," *Journal of Fluid Mechanics*, Vol. 525, 2005, pp. 275–308.

[6]Craig, S. and Saric, W., "Experimental Study of Crossflow Instability on a Mach 6 Yawed Cone," *AIAA Paper 2015-2774*, June 2015.

[7]Ward, C., Henderson, R., and Schneider, S., "Possible Secondary Instability of Stationary Crossflow Vortices on an Inclined Cone at Mach 6," *AIAA Paper 2015-2773*, June 2015.

[8]Moyes, A., Paredes, P., Kocian, T., and Reed, H., "Secondary Instability Analysis of Crossflow on a Hypersonic Yawed Straight Circular Cone," *AIAA Paper 2016-0848*, January 2016.

[9]Sweeney, C., Chynoweth, B., Edelman, J., and Schneider, S., "Instability and Transition Experiments in the Boeing/AFOSR Mach 6 Quiet Tunnel," *AIAA Paper 2016-0355*, January 2016.

[10]Muñoz, F., Heitmann, D., and Radespiel, R., "Instability Modes in Boundary Layers of an Inclined Cone at Mach 6," *AIAA Paper 2012-2823*, June 2012.

[11]Chynoweth, B. C., *A New Roughness Array for Controlling the Nonlinear Breakdown of Second-Mode Waves at Mach 6*, Master's thesis, Purdue University, School of Aeronautics and Astronautics, August 2015.

[12]Ward, C., *Crossflow Instability and Transition on a Circular Cone at Angle of Attack in a Mach-6 Quiet Tunnel*, Ph.D. thesis, Purdue University, December 2014.

[13]Berridge, D., *Generating Low-Pressure Shock Waves for Calibrating High-Frequency Pressure Sensors*, Ph.D. thesis, Purdue University, December 2015.

[14]Balakumar, P., "Stability of Supersonic Boundary Layers on a Cone at an Angle of Attack." *AIAA Paper 2009-3555*, June 2009.

[15]Ali, S. R. C., Wu, J., Radespiel, R., Schilden, T., and Schröder, W., "High-Frequency Measurements of Acoustic and Entropy Disturbances in a Hypersonic Wind Tunnel," *AIAA Paper 2014-2644*, June 2014.

[16]Heitmann, D., Kähler, C., Radespiel, R., Rödiger, T., and Krämer, E., "Disturbance-Level and Transition Measurements in a Conical Boundary Layer at Mach 6," *AIAA Paper 2008-3951*, June 2008.

[17]Steen, L. E., *Characterization and Development of Nozzles for a Hypersonic Quiet Wind Tunnel*, Master's thesis, Purdue University, School of Aeronautics and Astronautics, December 2010.

[18]Beresh, S. J., Henfling, J. F., Spillers, R. W., and Pruett, B. O. M., "Fluctuating wall pressures measure beneath a supersonic turbulent boundary layer," *Physics of Fluids*, Vol. 23, No. 7, 2011.

[19]Casper, K. M., Beresh, S. J., Henfling, J. F., Spillers, R. W., Pruett, B., and Schneider, S. P., "Hypersonic Wind-Tunnel Measurements of Boundary-Layer Pressure Fluctuations," *AIAA Paper 2009-4054*, June 2009.

[20]Stainbeck, P., Fischer, M., and Wagner, R., "Effects of Wind-Tunnel Disturbances on Hypersonic Boundary-Layer Transition," *AIAA Paper 1972-0181*, January 1972.

[21]Fedorov, A., "Transition and Stability of High-Speed Boundary Layers," *Annual Review of Fluid Mechanics*, Vol. 43, 2011, pp. 79–95.

[22]Wheaton, B. M., "Boundary Layer Stability on Circular-Arc Geometries at Mach 6," Tech. rep., Purdue University AAE 624 Final Report, December 2008.

[23]Marineau, E. C., Moraru, C. G., Lewis, D. R., Norris, J. D., Lafferty, J. F., and Johnson, H. B., "Investigation of Mach 10 Boundary Layer Stability of Sharp Cones at Angle-of-Attack, Part 1: Experiments," AIAA Paper 2015-1737, January 2015.

[24]Babinsky, H. and Harvey, J. K., "Shock Wave-Boundary-Layer Interactions," Cambridge University Press, 2014.

[25]Oberkampf, W. L., Aeschliman, D. P., Tate, R. E., and Henling, J. F., "Experimental Aerodynamics Research on a Hypersonic Vehicle," Sandia Report SAND92-1411, 1993.